Numerical model validation for mooring systems: Method and application for wave energy converters

Harnois, V., Weller, S.D., Johanning, L., Thies, P.R., Le Boulluec, M., Le Roux, D. Soulé, V., Ohana J.

Abstract

Mooring systems are key sub-systems of wave energy devices. The design of mooring systems is challenging because overdesign of the mooring system incurs a significant cost penalty, while underdesign may lead to a premature failure. Incorrect design could also reduce the power production. It is therefore important to develop mooring systems which are specific for wave energy applications.

Appropriate mooring solutions can only be developed if numerical models are sufficiently validated with data from physical experiments. This paper presents tank test results for a scale model of the buoy and mooring used at the South West Mooring Test Facility (SWMTF), an offshore facility developed to conduct long-term sea trials for wave energy device moorings. Preliminary static, quasi-static, decay, regular and irregular wave tests were conducted on the 1:5 scale model, using the Ifremer basin in Brest. A corresponding numerical model was developed with a time-domain mooring modelling tool, inputting hydrodynamic data from a radiation/diffraction potential modelling program.

After the calibration of several hydrodynamic parameters (added mass, damping and mean drift), the numerical model demonstrated good agreement with the experiment, providing an accurate prediction of the maximum mooring loads in irregular waves. The methods and procedures presented will allow the effective validation of numerical models to enable the development of appropriate mooring systems in wave energy applications.

Keywords: tank tests, mooring, Wave Energy device, numerical model, fibre rope

1. Introduction

The survivability of a wave energy device is dependent on the structural integrity of the mooring system, which represents an estimated 5% of the cost of energy [1] and of the capital costs for a farm [2]. Total or partial failure of the mooring system may lead to the loss of the device. This risk must be balanced with the cost of an over-engineered design.

Wave energy mooring systems do have specific requirements [3]. In particular motion-dependent devices need to have compliant mooring lines to avoid large mooring loads or adverse effects on power production. This requirement can e.g. be satisfied by synthetic fibre ropes. At the same time the mooring system should limit the horizontal excursion of the floating body to avoid tension on the power cable or collisions between devices in an array, for example by providing restoring forces with a catenary mooring system.

The main aim of early stage tank tests is often to validate concepts and to improve the performance of the Power Take-Off (PTO) system [4]. Consequently, the mooring system is commonly represented in a simplified form which does not significantly influence the behaviour of the PTO system [5] and/or the limited water depth in the tank does not allow the moored model to be scaled correctly [6]. However, it is crucial that the influence of the mooring system on PTO performance is taken into account at a more advanced stage. For example in [7], the power production for the DEXA wave energy device was compared for two types of mooring system: Catenary Anchor Leg Mooring (CALM) and spread mooring. Different catenary configurations-with different attachment points and/or the use of additional surface buoys were also compared in term of power production in [8].

This paper draws on tank tests that were conducted using a scale model of the buoy and mooring used at the South West Mooring Test Facility (SWMTF). The SWMTF research is led by the Renewable Energy group at the University of Exeter and was initiated through funding provided through the Peninsula Research Institute for Marine Renewable Energy (PRIMaRE). This facility has been built to conduct long-term sea trials for the mooring systems of marine energy devices. It is installed in Falmouth Bay, Cornwall, UK, in a site with a water depth between 27 and 32.4m, depending on tidal elevation. This facility has been previously described in [9]-[11]. The highest observed significant wave height *Hs* was 3.5m and the most

frequent sea states were for *Hs* equal to 0.8 m and *Tp* equal to 6s. At the SWMTF, an instrumented surface buoy of mass *M*=3250 kg is moored with a three catenary leg mooring system combining chains and nylon rope. The axial stiffness (EA with *E* the Young's Modulus and *A* the sectional area of the rope) of dry nylon rope used as part of the SWMTF mooring system was measured from tension-tension tests conducted using the Dynamic Marine Component (DMaC) facility at the University of Exeter [12]. For a range of harmonic loading regimes with mean loads and amplitudes not exceeding 1.0% and 0.6% respectively of the Minimum Breaking Load (MBL), the rope sample demonstrated axial stiffness values between 889-972kN for oscillation periods ranging from 25 to 100s.

This paper is divided in 5 sections, including introduction. Section 2 will describe the experimental set-up and the numerical modelling of the mooring system. Section 3 gives results from static and quasi-static tests, decay tests, as well as regular and irregular wave tests. The results are discussed in section 4 followed by a conclusion in section 5.

2. Experimental set-up and modelling of the mooring system

This section describes the experimental set-up and the numerical modelling of the mooring system. The properties of the basin and its instrumentation are described, the choice of scale is explained, and the scaled properties of the buoy and its mooring are detailed. Finally, the inputs of the numerical model are defined.

2.1 Experimental set-up

The tank tests were performed in the Ifremer deep water wave basin, in Brest, France. This tank uses sea water with a density of 1.026 kg/m^3 at 17.2°C, and 35.6% salinity (averages based on three sample measurements during the test period using the method described by Sharqawy [13]). The basin is 50m long, 12.5m wide and 10m deep for the first three quarter of its length, where the model is installed. The wave generator is able to generate waves with a maximum amplitude of 0.5m and with periods from 0.8 to 3.5 s. The mooring loads were recorded with axial load cells installed on the top of each mooring line. Six degree-of-freedom motions at the buoy centre of gravity were determined using a Qualysis™ video motion tracking system with reflecting targets mounted on the top of the buoy (Fig. 1 (a)). Surface elevations were measured with servo wave gauges, installed as shown in Fig. 1 (b). All measured signals were time synchronised and recorded at 100Hz.

The scale of the model was determined by the dimensions of the tank, particularly its width. An initial full-scale static numerical investigation with Orcaflex™ was carried out to estimate the length of mooring line constantly resting on the seabed for a range of surge/sway (+/-30m) and heave (+/-15m) buoy motions. These motions were the largest observed motions during the sea trials of the SWMTF. The portion of mooring line which rests on the seabed during large displacements does not significantly interfere with the hydrodynamic behaviour of the system and can therefore be truncated. The results of this preliminary study indicated that a Froude model scale of 1:5 with a water depth of 5.95m was feasible. A false floor was installed in the tank to achieve the desired water depth (Fig. 1 (c)). Truncated mooring lines were simplified and scaled as indicated in Table 1. For example, Section 4 of the mooring is at the full scale facility made of a DN24 openlink chain and of a 9.5 tonnes shackle. In the scale model only a chain was used, taking into account the weight of the shackle. The drag and inertia coefficients and the seabed friction for the mooring lines were taken from DNV standards [14] for the nylon lines and from the Orcaflex™ manual [15] for the chains. The axial stiffness of three samples extracted from the used SWMTF rope was quantified using tension testing equipment at Ifremer [16]. The yarns demonstrated axial stiffness values between 10.0 and 12.6kN when subjected to scaled (by N/Tex) loading using a 25s oscillation period. An average value of 10.873kN was used in the numerical model, which is slightly different from the scaled stiffness of the full scale facility.

The model was oriented with mooring lines 1 and 3 facing the wave symmetrically (Fig. 1 (b)), and all tests were carried out with a wave incidence angle equal to zero. Table 2, which is based on [17] gives details about the scale model properties, and the differences between the theoretical scaled values and the measured scaled values. Fig. 1 (a) illustrates the dimensions of the scaled buoy.

Table 1 Properties of the original mooring lines and of the simplified, scaled and truncated mooring lines. Cd_n and Cm_n are normal coefficients, Cd_a and Cm_a are axial coefficients, T stands for tonnes, DN for nominal diameter

Section: top(1) to bottom (4)	Section simplified mooring	Components of full scale SWMTF mooring	Length (m)	Ø (m)	Mass (kg/m)		Axial stiffness (*EA*, N)	Drag coefficient		Inertia coefficient	
					In air	In water		Cd_n	Cd_a	Cm_n	Cm_a
1	Chain	Swinging arm 4x9.5T shackle rope thimble load cell 10T swivel 25T shackle large rope thimble	0.259	0.008	1.753	1.529	6.464e6	1	0.4	1	0.07
2	Rope	Nylon rope: Bridon superline 44mm diameter	4.0	0.009	0.024	0.00425	Scaled value for full scale facility: 7.1-7.8 e3 Tank (mean): 1.0873e4	1.6	0	1	0
3	Chain	2x9.5T shackle 10T swivel 25T shackle large rope thimble	0.126	0.006	1.786	1.558	3.636e6	1	0.4	1	0.07
4	Chain	DN24 openlink chain 9.5T shackle	5.672	0.0049	0.4609	0.402	2.0505e6	1	0.4	1	0.08

Table 2 Full scale and model buoy properties and difference with theoretical values. COG=centre of gravity

	Full scale SWMTF values	Theoretical scaled values	Measured scaled values	Relative error
Mass (kg)	3108	24.86	24.86	0%
Distance between COG and bottom of keel (m)	1.13	0.2260	0.2262	0.09%
I_{xx} (kg.m^2)	4260.75	1.3634	1.4141	3.72%
I_{zz} (kg.m^2)	1178.83	0.3772	0.3963	5.06%

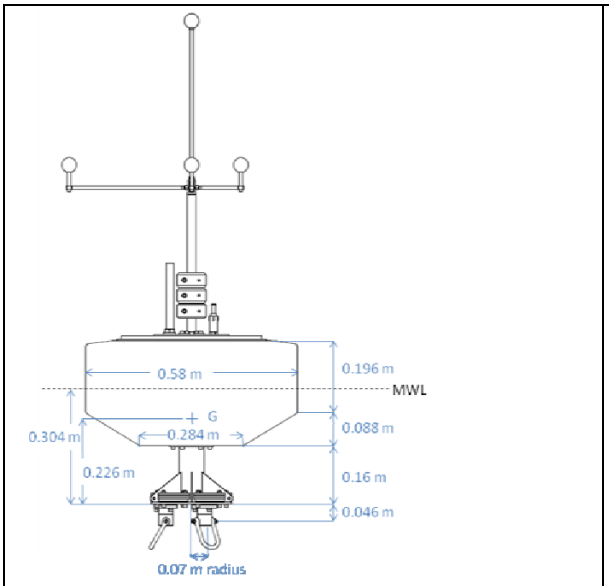

(a)

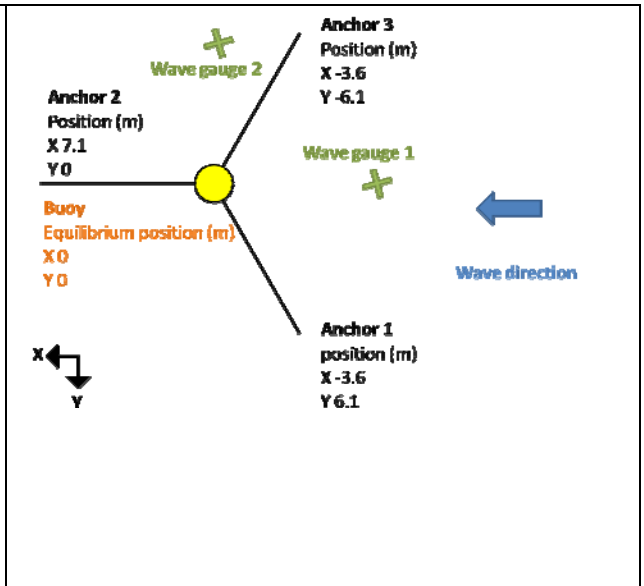

(b)

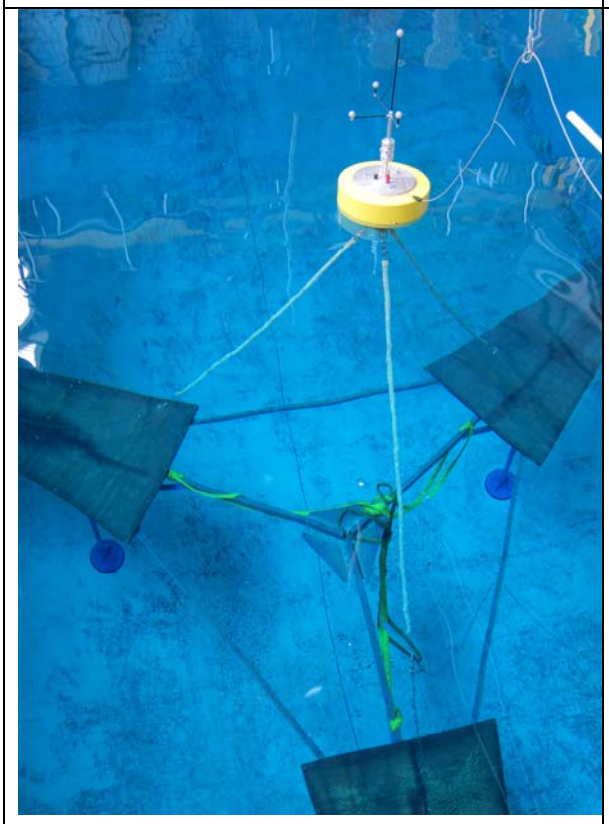

(c)

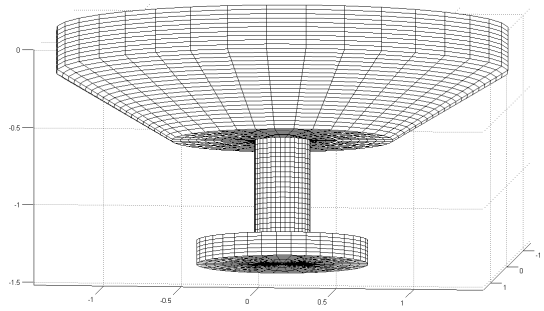

(d)

Fig. 1 Wave basin installation and numerical model settings: a) Side view of the buoy and dimensions, b) Top view of the truncated mooring and of the wave gauge layout, c) Photograph of the SWMTF model in the basin, with the false floor, d) Buoy hull mesh used for the radiation/diffraction potential analysis

2.2 Modelling of the mooring system

Mooring system software such as Orcaflex™ requires the specification of hydrodynamic parameters. Hydrostar™, a radiation/diffraction potential code, was used to calculate the hydrodynamic properties for a simplified hull shape (Fig. 1. (d)) and for each wave frequency, from 0.11 to 13.42rad/s, in increments of 0.11rad/s. This simplified shape does not include the vertical triangular braces at the bottom of the buoy (Fig. 1 (a)), therefore the added mass and hydrodynamic damping associated with these features are not accounted for. The frequency-dependent data calculated for each of the 6 degrees of freedom of the buoy were: a) the load Response Amplitude Operators (RAOs) and associated phases at the metacentre at the equilibrium of the buoy, b) the added masses at the centre of gravity (COG) of the buoy, c) the radiation damping values at the COG of the buoy, and d) the Quadratic Transfer Functions (QTFs) at the metacentre at the equilibrium of the buoy. The viscous damping cannot be calculated by radiation/diffraction potential codes.
To simplify the Orcaflex™ calculations, Newman's approximation was used for the QTFs. This approximation is valid because the deep water theory can be used, as confirmed by the Ursell number [18].

$$Ur_{\max} = \frac{H_{\max}\lambda_{\max}^2}{8\pi^2 h^3} = \frac{0.5 \times 5.2^2}{8\pi^2 5.95^3} = 0.00081 << 1 \qquad (1)$$

With H_{max} the highest wave height used for regular wave tests, λ_{max} the highest wave length used for regular wave tests and h the water depth.

3. Validation results

This section will present results from the different tests. As shown in Fig. 2, each test will provide different information about the hydrodynamics of the buoy and its mooring. This information will then be used to finely calibrate the numerical model and correct potential inaccuracies. The aim of this serie of tests is to obtain an accurate model in realistic sea states.

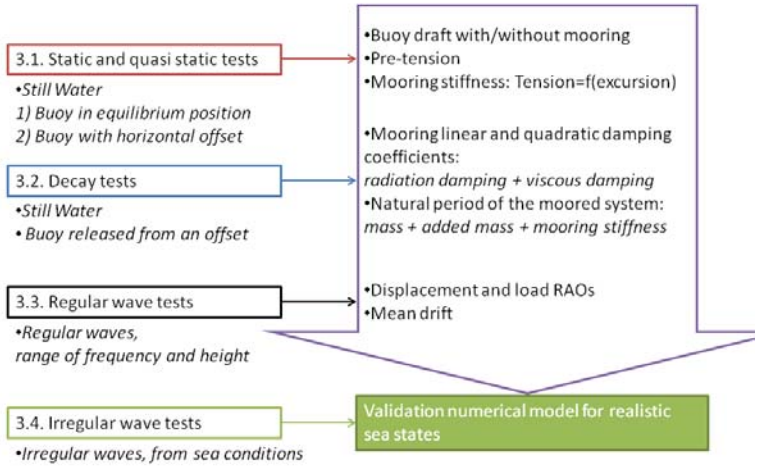

Fig. 2 Range of tests needed to validate a numerical model with experimental data

3.1 Static and quasi static tests

Static tests were conducted in still water conditions to determine the buoy draft, with and without mooring lines in place. In free-floating conditions, before attaching the mooring lines, the centre of gravity of the buoy was at 0.078m below the mean water level in the basin. This distance was set in the numerical model. After the attachment of the mooring lines, the centre of gravity was 0.10m below the mean water level and the mooring pre-tension was 18N in both the basin and the numerical model.

Quasi-static tests were used to identify the horizontal stiffness characteristics of the mooring system, by determining the relationship between buoy horizontal position and mooring line tension. The model was placed in the basin and mooring tensions were measured in still water conditions for several buoy surge offset positions.

The results of the quasi-static tests are presented in Fig. 3 (a), indicating the tension in the mooring lines for a given surge offset. The results of the tank tests and of the numerical model show an excellent agreement with a relative error not exceeding 6% (Fig. 3 (b)).

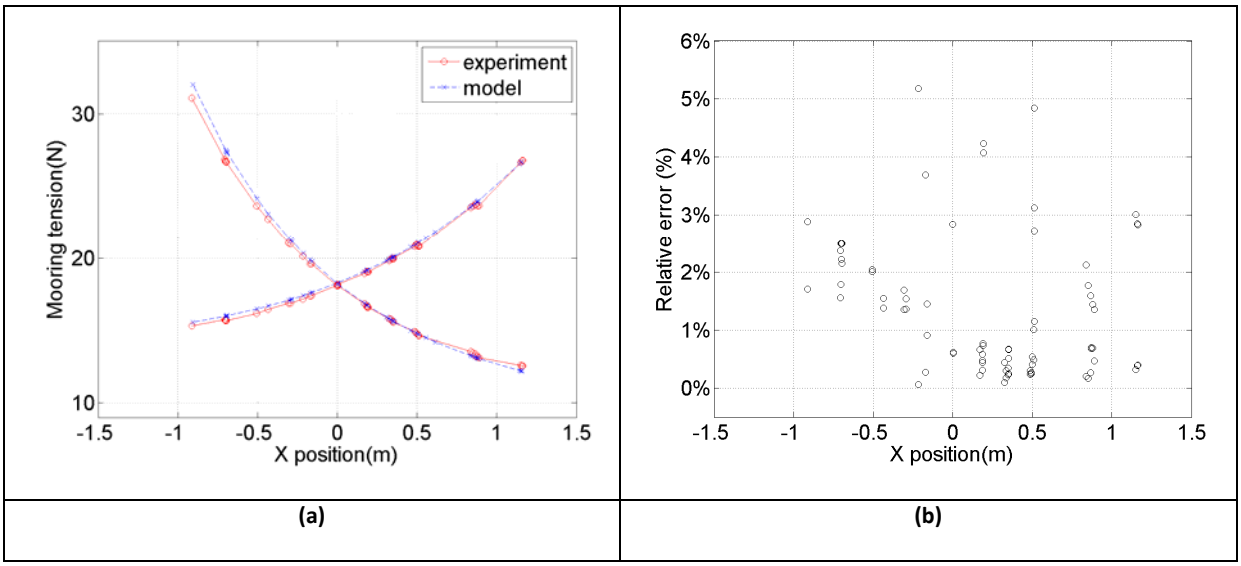

Fig. 3 Mooring stiffness: a) comparison of the experimental (red o) and modelled (blue x) mooring load/buoy surge offset relationships and b) relative error in mooring tension between experimental and modelled values

3.2. Decay tests

Decay tests were carried out to evaluate the radiation and viscous (drag) damping and the added mass of the buoy by calculating linear and quadratic damping coefficients and natural period. Decay tests involved moving the moored buoy from its equilibrium position in one degree of freedom and then releasing it. The buoy is moving at its natural frequency for this degree of freedom, and the amplitude of motion is decreasing because of the damping of the system. A Matlab™ code called Wave Analysis for Fatigue and Oceanography, usually referred as WAFO [19] was used to detect peak and trough in the decay time series. The first decay oscillation was ignored for calculation, because the buoy may have experienced additional damping due to the release of the mooring. The 5 next peaks and the 5 next troughs of each decay tests were used to calculate the natural period and damping coefficients. The amplitude of release used for the numerical model was the mean amplitude after the first oscillation during the tank tests. The amplitudes of release and after one oscillation during tank tests are given in Table 3 and Table 4.

The natural period depends mainly on the stiffness of the moored system, its mass and added mass. Quasi static tests indicated that the stiffness of the mooring system in the numerical model is very close to the experimental model, and the model buoy was weighed before the tank tests, as shown in Table 2, with a perfect agreement between the experimental and numerical values. This means that the natural period will validate the value of added mass calculated by the radiation-diffraction code. The natural period was calculated as the mean time between similar extreme values (peak or trough).

The radiation damping forces depend linearly on the magnitude of relative velocity of the sea past the buoy, and the viscous damping in a quadratic way. The overall damping was calculated for the tank tests and for the numerical model, and was separated into a linear and a quadratic coefficient: $p_1 + p_2\left|\xi_j\right| i\omega$, with ξ_j the motion amplitude in one degree of freedom and ω the angular frequency. p_1 and p_2 can be calculated using the relation described by Faltinsen [20], assuming the damping to be constant with respect to the oscillation amplitude:

$$\frac{2}{T_m}\log\left(\frac{X_{n-1}}{X_{n+1}}\right) = p_1 + \frac{16}{3}\frac{X_n}{T_m}p_2 \qquad (2)$$

Where X_n is the amplitude of the nth oscillation and T_m the natural period of oscillation. Fig. 4 (a) and (b) illustrate this method: a) extremes are detected, and b) $\frac{2}{T_m}\log\left(\frac{X_{n-1}}{X_{n+1}}\right)$ is plotted against $\frac{16}{3}\frac{X_n}{T_m}$, allowing the calculation of *p1* and *p2* by linear regression using a least squares method. The norm of the residual was calculated to give an indication of the goodness of the fit.

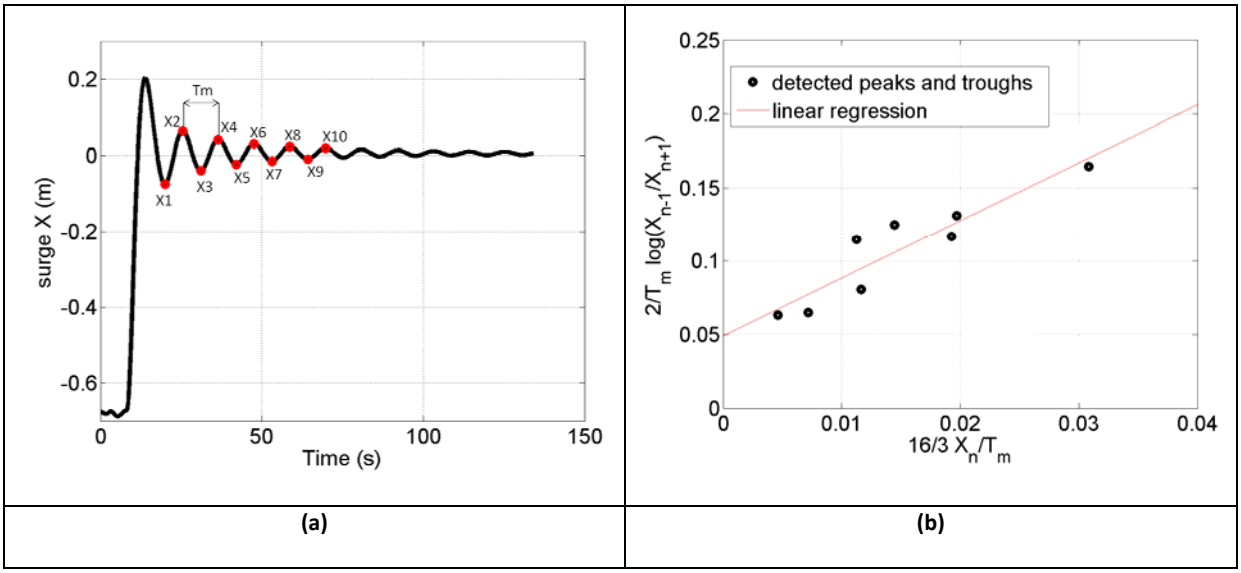

(a) **(b)**

Fig. 4 Example of calculation of the natural period and linear and quadratic damping: a) detection of peaks and troughs and calculation of the natural period, b) calculation of the linear p_1 and quadratic p_2 damping coefficients using a linear fit; norm of the residual=0.036

Decay results from the tank tests and from the initial numerical model are presented in Fig. 5 (a) and (b) and Table 3-Table 5. Test repeatability was evaluated using the standard deviations of natural period, damping coefficients and norms of the residuals between the different experiments. Table 3 indicates that for the different surge decay tests, similar results were obtained for the natural period and the quadratic damping coefficients, and more variability was observed for the linear damping coefficients. Because of this repeatability, the values chosen to calibrate the numerical model are the mean values of natural period and damping coefficients over the 6 experiments. The pitch decay tests provide a larger range of natural period and damping values for the different experiments. This lack of repeatability may be due to a coupling of the pitch motion with the surge motion, as seen in Fig. 5 (b). In these cases, large amplitudes of the surge motion-up to 0.4m- are observed and the pitch motion does not oscillate around zero. Because of this lack of repeatability, the pitch motion properties could not be evaluated accurately and the experimental values could not be used to calibrate the numerical model.

The initial numerical model was underestimating the damping of the system and the natural period in surge (Fig. 5 (a), Table 5). The inaccuracies in the added mass and linear damping may have been due to the simplified shape or the inabilities of evaluating quadratic damping of the radiation-diffraction model. Following an iterative process, the added mass, linear and quadratic damping values were adjusted until the numerical natural periods and damping coefficients matched the experimental values:

a) The surge added mass is multiplied by coefficients between 1 and 1.5 for all the wave frequencies and simulations are run with these corrected added masses; the natural period is calculated for each added mass simulation and plot against the multiplying coefficients (Fig. 6 (a)). A linear fit gives the value of multiplying coefficient which leads to a similar natural period than the experimental one.

b) Additional quadratic damping value is added to the numerical model with values between 0 and the total quadratic damping value p2 calculated from the tank tests and simulations are run with this additional damping. The quadratic damping coefficient p2 is calculated for each simulation and plotted against the additional quadratic damping (Fig. 6 (b)). A linear fit gives the value of additional damping which leads to a similar quadratic damping p2 than the experimental one.

c) Additional linear damping is slowly increased in the numerical model. For each value of additional linear damping, the linear damping coefficient p1 is calculated and plotted against the value of additional linear damping (Fig. 6 (c)). Following a similar method than for the additional quadratic damping, a value of additional linear damping is chosen for further calculations.

Calibrations are summarised in Table 6. For the surge, the corrected model shows a good agreement with the experimental data, as seen in Fig. 5 (a) or Table 5, with less than 8% relative error between the measured and modelled natural periods and damping values.

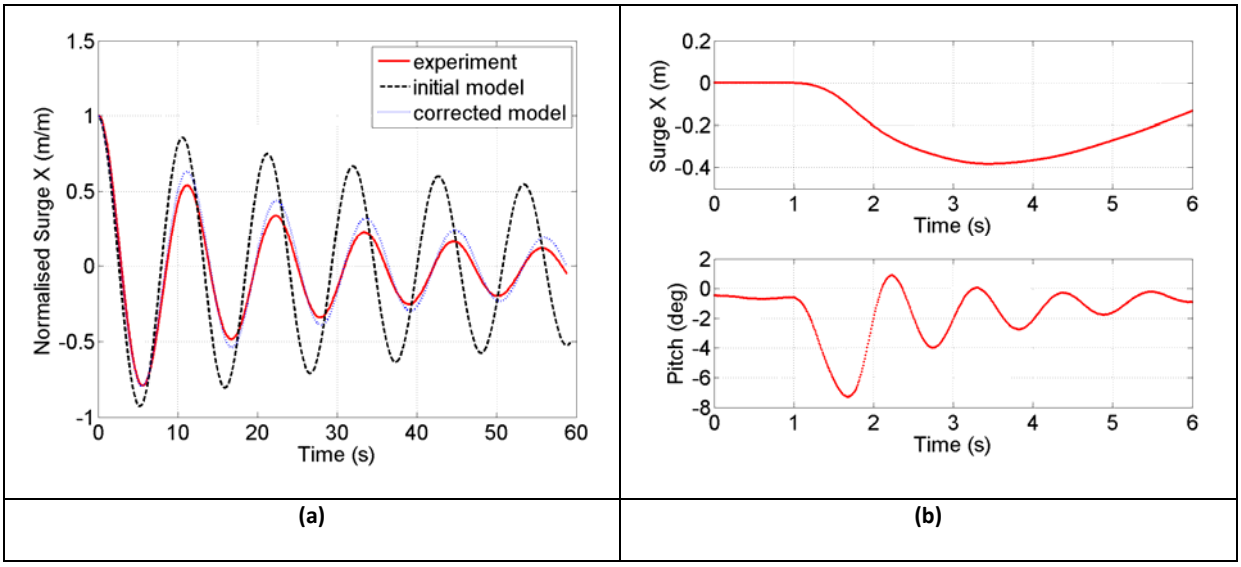

Fig. 5 Time-series of decay tests in a) surge, with comparison with initial and corrected numerical models and b) pitch, with a plot of the surge motion to show the coupling between surge and pitch.

Table 3 Results for the surge decay tests: amplitude of release and after one oscillation, natural period T_m, linear damping p_1 and quadratic damping p_2, and norm of the residuals associated with the damping linear fit

		Surge	Mean	Standard deviation
Amplitude of release(m) / amplitude after 1 oscillation (m)	Exp. 1	-0.69/-0.076	Mean(abs)=0.70/0.084	Std(abs)=0.075/0.0078
	Exp. 2	-0.59/-0.083		
	Exp. 3	-0.82/-0.074		
	Exp. 4	0.70/0.092		
	Exp. 5	0.67/0.090		
	Exp. 6	0.73/0.090		
Natural period T_m (s)	Exp. 1	11.06	**11.11**	0.0447
	Exp. 2	11.09		
	Exp. 3	11.11		
	Exp. 4	11.14		
	Exp. 5	11.10		
	Exp. 6	11.19		
p_1 (s^{-1})	Exp. 1	0.03133	**0.0393**	0.0127
	Exp. 2	0.02737		
	Exp. 3	0.02688		
	Exp. 4	0.04234		
	Exp. 5	0.05554		
	Exp. 6	0.05249		
p_2 (m^{-1})	Exp. 1	4.876	**5.0949**	0.3036
	Exp. 2	4.643		
	Exp. 3	5.119		
	Exp. 4	5.227		
	Exp. 5	5.523		
	Exp. 6	5.181		
Norm of the residuals	Exp. 1	0.05360	0.1041	0.0750
	Exp. 2	0.03701		
	Exp. 3	0.03732		
	Exp. 4	0.1121		
	Exp. 5	0.2150		
	Exp. 6	0.1697		

Table 4 Results for the pitch decay tests: amplitude of release, natural period T_m, linear damping p_1 and quadratic damping p_2, and norm of the residuals associated with the damping linear fit

		Pitch	Mean	Standard deviation
Amplitude of release(deg) / amplitude after 1 oscillation (deg)	Exp. 1	-7.3/-4.0	Mean(abs)=3.7/2.3	Std(abs)=2.1/1.1
	Exp. 2	-3.0/-2.1		
	Exp. 3	-3.6/-2.4		
	Exp. 4	-3.2/-2.2		
	Exp. 5	1.6/0.93		
Natural period T_m (s)	Exp. 1	*1.070*	/	/
	Exp. 2	*1.080*		
	Exp. 3	1.095		
	Exp. 4	*1.120*		
	Exp. 5	1.088		
p_1 (s^{-1})	Exp. 1	/	/	/
	Exp. 2	/		
	Exp. 3	-0.5105		
	Exp. 4	/		
	Exp. 5	0.01242		
p_2 (rad^{-1})	Exp. 1	/	/	/
	Exp. 2	/		
	Exp. 3	0.9197		
	Exp. 4	/		
	Exp. 5	0.3268		
Norm of the residuals	Exp. 1	/	/	/
	Exp. 2	/		
	Exp. 3	0.8512		
	Exp. 4	/		
	Exp. 5	0.1585		

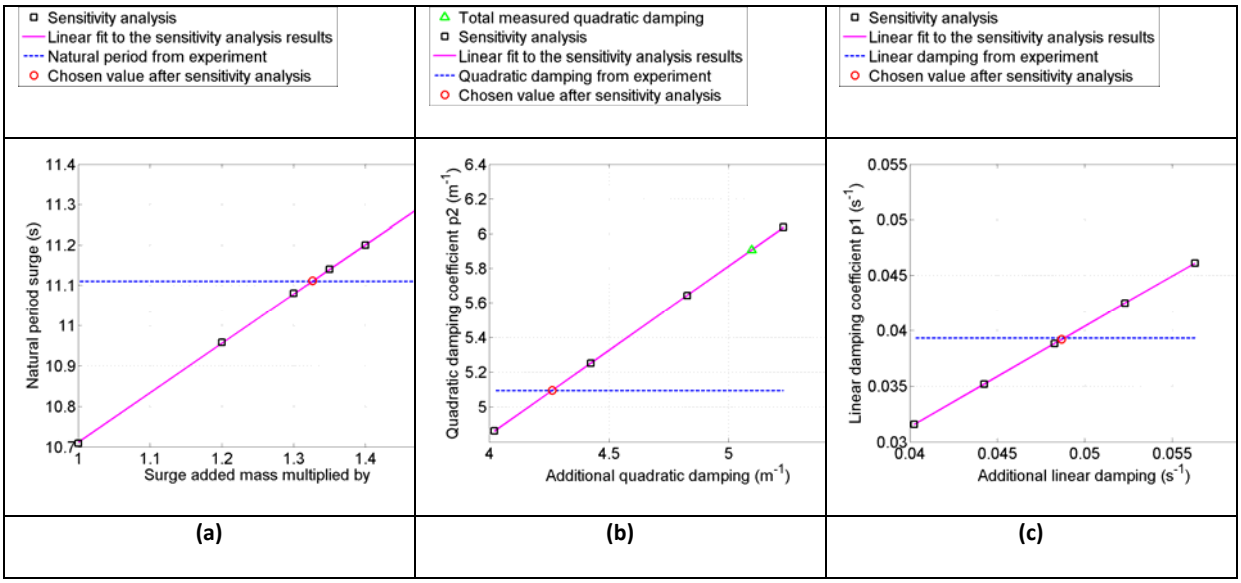

Fig. 6 Sensitivity analysis for the surge decay a) for the added mass; b) for the quadratic damping; c) for the linear damping

Table 5 Comparison of experimental and numerical results: natural period T_m, linear damping p_1 and quadratic damping $p_2$for surge decay

	Values measured from tank	Initial numerical model: value/relative error	Corrected numerical model: value/relative error
Surge			
Natural Period T_m (s)	**11.11**	10.68/4%	11.20/1%
p_1 (s^{-1})	**0.0393**	0.0008/98%	0.0426/ 8%
p_2 (m^{-1})	**5.0949**	1.0503/79%	4.7488/7%

Table 6 Correction implemented on added mass, linear damping p_1 and quadratic damping p_2 for the surge degree of freedom

	Added mass multipliedby	Additional Linear damping p_1 (s^{-1})	Additional Quadratic Damping p_2(m^{-1})
Surge	1.3262	0.0487	4.2639

3.3. Regular waves tests

Regular wave tests aim to evaluate Response Amplitude Operators (RAOs) of the buoy motions together with the mean drift for a large range of wave periods and wave steepness values. The RAOs are transfer functions indicating the response of the buoy in each degree of freedom for a range of wave frequencies. The damping of the pitch motion will also be assessed.

A total of 36 different tests were carried out using sinusoidal waves with wave periods and wave heights respectively from 0.88s to 2.3s and from 0.03m to 0.5m as shown in Fig. 7 (a). These tests correspond to waves with a period from 1.97s to 5.14s and a height from1.5m to 2.5m at full scale, which are operational sea states at the SWMTF site, and not extreme sea states. The choice of wave period and wave frequency was limited by the wave-breaking limit (H/λ=0.14 in deep water with H the wave height and λ the wave length) as well as the performance of the tank. Steep waves were defined as (Fig. 7 (b), [21]):

$$K_C > \frac{1}{2}\frac{0.14\pi\lambda}{D} \qquad (3)$$

With K_C the Keulegan-Carpenter number, and D the buoy diameter.
Steep waves (filled circles in Fig. 7 (a)) were used to observe non-linear behaviour, while waves with small amplitudes were used to determine the validity of response predictions based on linear wave theory. Wave periods near the resonance periods of the system were particularly investigated. The tests were run for at least 10 wave periods in order to observe the steady response of the floating structure.

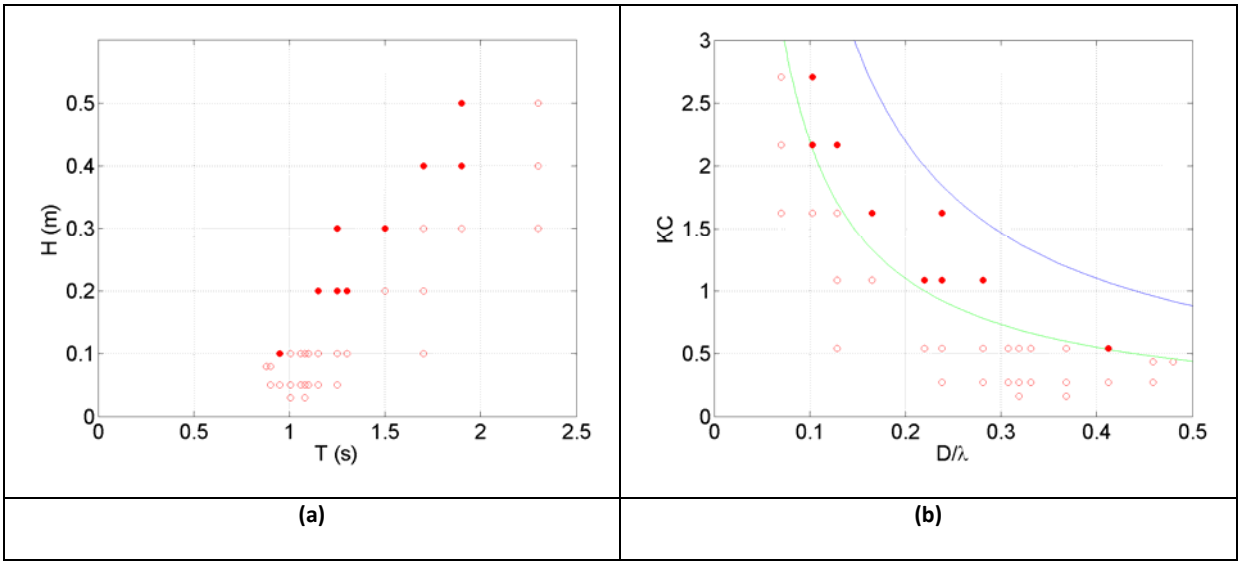

(a) (b)

Fig. 7 Review of tests in regular waves. a) Wave heights *H* and wave periods *T* used for the tank tests. b) Selection of steep waves, the green line is for $K_C = \frac{1}{2}\frac{0.14\pi\lambda}{D}$, separating the steep and the linear waves, and the blue line for $K_C = \frac{0.14\pi\lambda}{D}$, separating steep waves and breaking waves. The filled circles indicate steep waves.

Time series of experimental and modelled wave elevations and buoy motions are analysed using a least squares fit method to estimate the amplitude, period and phase. Basically, this means that the time-series are fitted to a cosine as described in equation (4) and shown in Fig. 8 (a). The mean of the motion, which is also the mean drift, was removed before the fit. The covariance is used as a correlation coefficient and was calculated between the original data and the fitted curves.

$$Wavefit(t) = A_w \cos(\omega_w t + \varphi_w)$$

$$Motionfit(t) = A_m \cos(\omega_w t + \varphi_m) \qquad (4)$$

For the initial numerical model, very good agreement was achieved for the heave, pitch and the waves, with values over 99% for the correlation coefficient between the data and the fit for the numerical and experimental heave, and over 83% for the pitch. The only fit which has a significantly lower correlation coefficient was for the experimental surge motion, with correlation values down to 42% for combinations of low wave periods and wave heights as shown in Fig. 8 (b). In these cases, a low frequency surge motion was observed in the tank (Fig. 8 (c)), and the mean drift presents some inaccuracies. This low frequency motion may have been due to wave reflection on the walls of the basin. The solution to validate the fit was to filter the surge motion with a moving average using 250 points. The filtered data and the fit show correlation coefficients over 97%, which validates the fit.

The RAOs were then calculated as A_m/A_w and the associated phases as φ_m-φ_w. The mean drift was divided by the square of the wave amplitude because the drift forces are proportional to the wave amplitude squared.

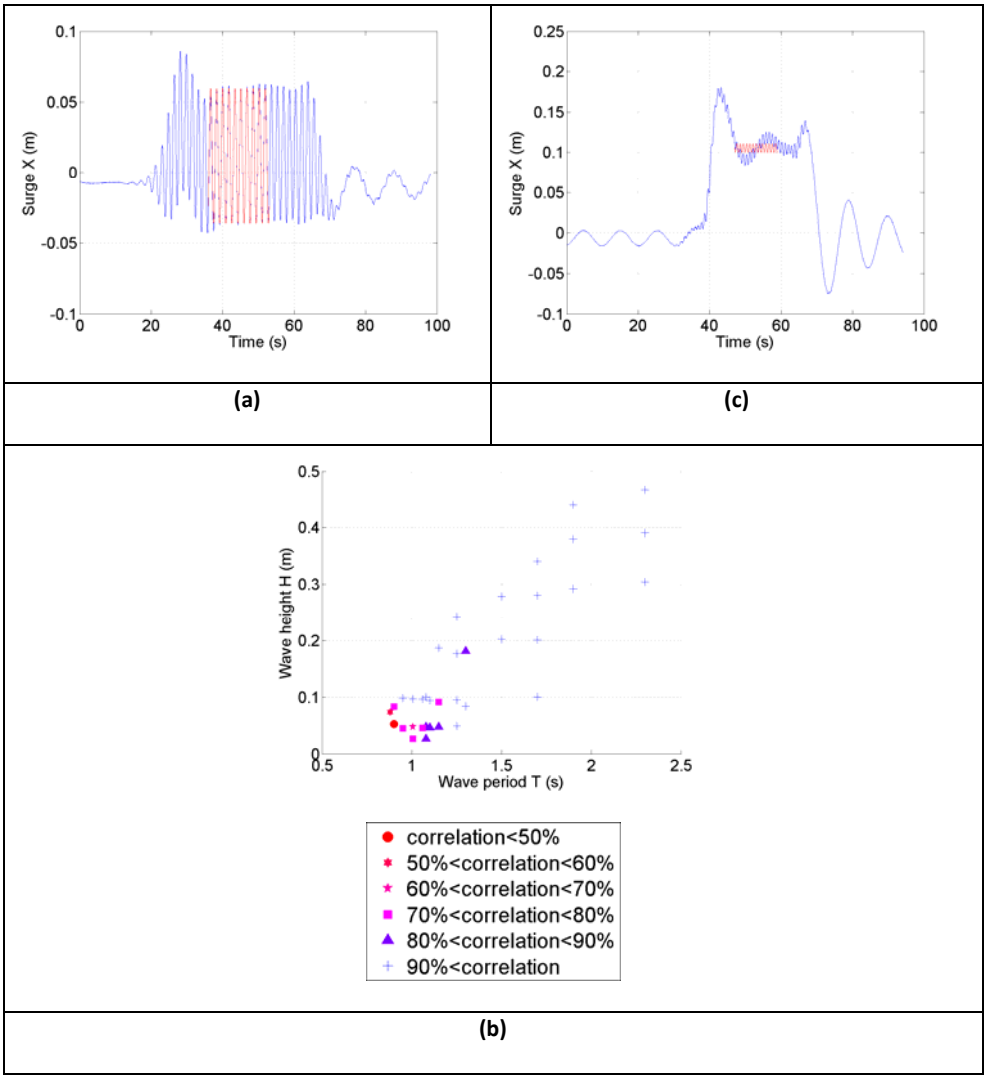

Fig. 8 Examples of fit of the experimental surge motion a) for *H*= 0.1m and *T*= 1.7s; b) Summary of the correlation coefficient between the fit and the experimental values c) for *H*=0.05m and *T*= 0.9s where a low frequency motion on the X axis can be observed;

Results for the regular waves are presented in Fig. 9 (mean drift) and Fig. 10 (motion RAOs and phases). Red circle markers indicate values measured during the experiment and black diamond markers values calculated by the initial numerical model. Filled markers are used for data obtained with steep waves, as defined previously.

Results indicate that for wave frequencies over 0.9Hz, the modelled mean drift (Fig. 9) was underestimated by the initial numerical model and actually appeared to decrease between 0.9 and 1Hz for the initial numerical model, with a minimum value at 19-20 m/m^2 at 1Hz while the experimental values are between 40 and 44 m/m^2 at 1Hz. This inaccuracy originates from the potential radiation-diffraction code which outputs mean drift forces with this shape. A methodology to correct the QTF will be proposed below.

The main result from the RAO analysis is that the initial modelled pitch RAOs are largely overestimating the pitch RAOs around the resonant frequency f=0.9Hz. The maximum modelled value at this frequency was approximately 900deg/m while the maximum experimental value was approximately 525deg/m. This is due to the lack of damping in pitch, with viscous damping forces not considered in the numerical model at this stage as described in the previous section. A methodology to add viscous damping will be proposed below.

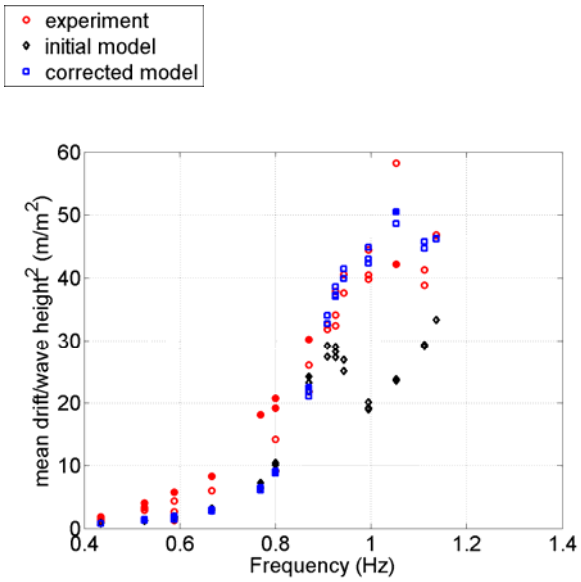

Fig. 9 Mean drift divided by the square of the wave amplitude for different wave frequencies and wave steepness values.

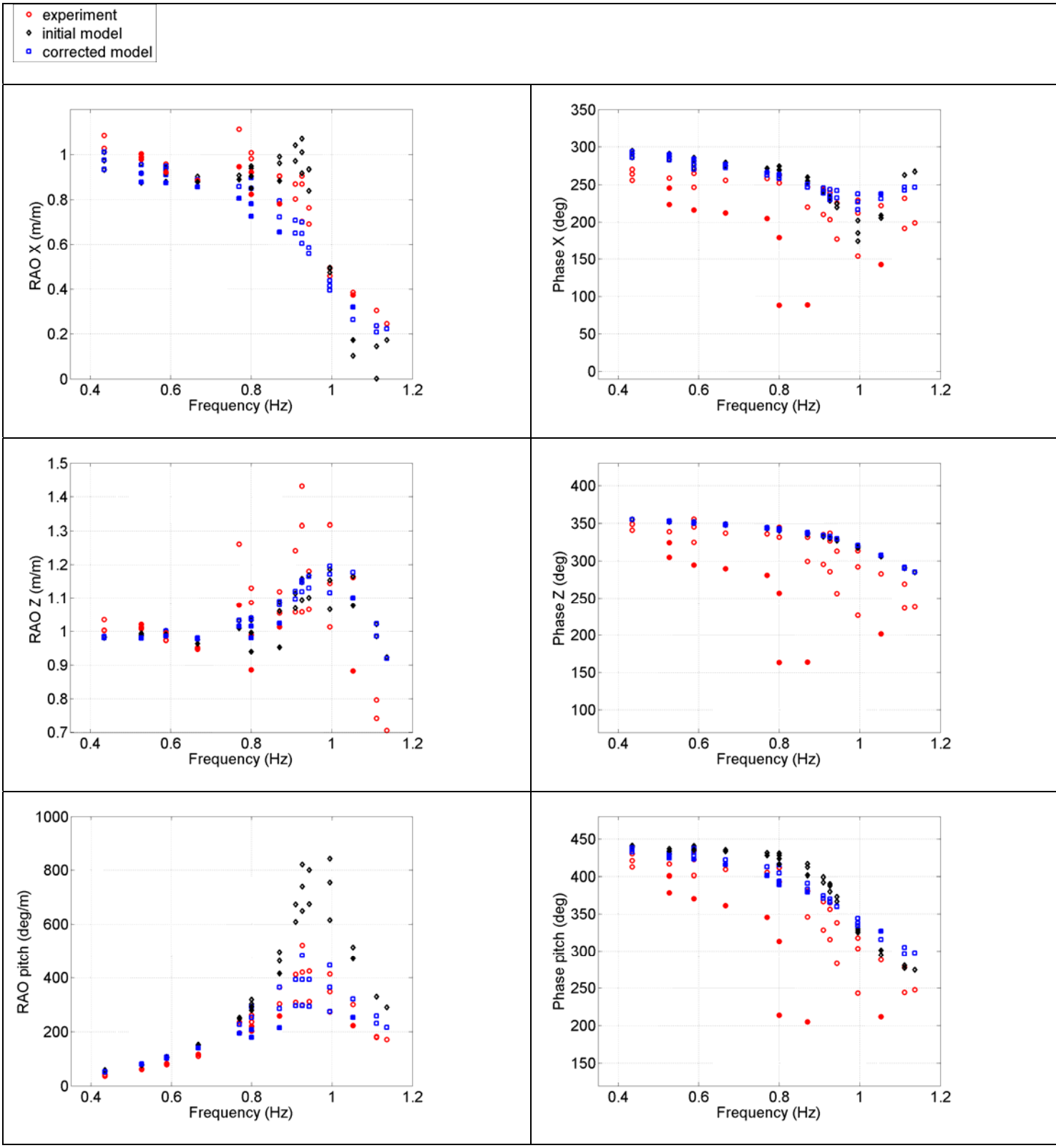

Fig. 10 Motion RAOs for the surge, heave and pitch (from top to bottom): amplitudes (left) and phases (right)

Calibration of the QTFs

The mean drift values were corrected by calibrating the QTF values (Fig. 11):

a) the QTFs are multiplied by different coefficients between 0.5 and 10. Each tank test is replicated in the numerical model for the different input values of QTFs and mean drifts are calculated.

b) For each test over 0.85Hz, the difference between the mean drift for the experiment and for the numerical model is plotted against the different QTF multiplying coefficients. A linear fit is applied and the value to cancel the difference is output.

c) The values to cancel the difference in each test is plotted against the wave frequency. A smoothing spline is fitted to these values, and interpolated multiplying coefficients are output.

d) The initial QTF is multiplied by the interpolated multiplying coefficients, and to avoid jump in the data, data are linearly interpolated.

However, for wave frequencies outside of the range used in this study, the validity of the modelling of the mean drift is not known. For low frequencies, the difference of mean drift between the numerical model and the experiment tends towards zero, but for high frequencies, further investigations are required to validate the modelling of the mean drift. Once the numerical model has been corrected the experiment (red circles) and the model (blue squares) were giving similar results in the considered range of steep and linear waves (Fig. 9).

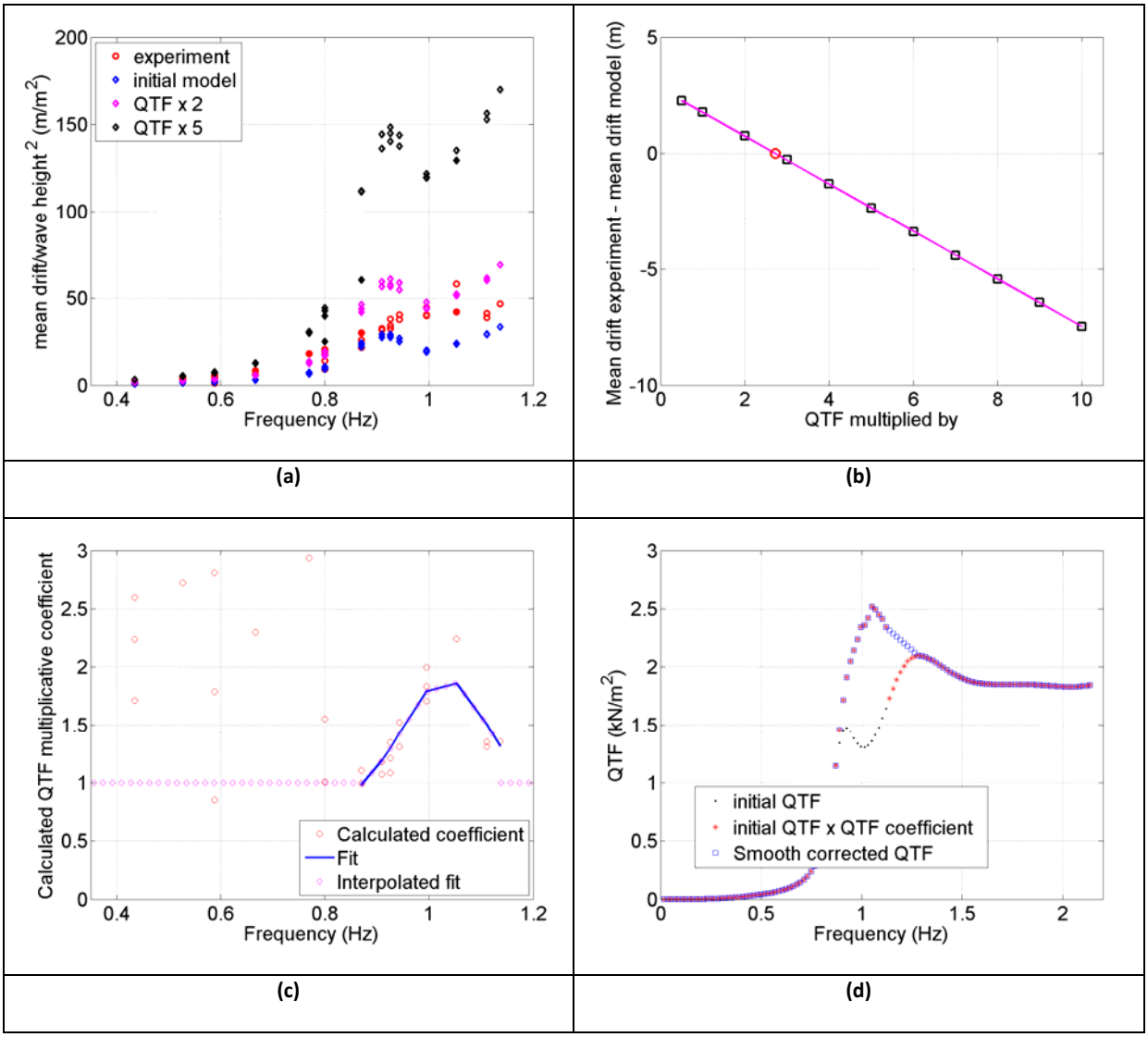

Fig. 11 Sensitivity analysis for the surge QTF for the linear waves a) calculation of the mean drift for different multiplicative factors of the QTF for all sea states b) for a given sea state, calculation of the corrective multiplicative factor which leads to similar mean drift for the experiment and the numerical model (here for H=0.6m and T= 1.9s); c) for frequencies over 0.85Hz, fit of the corrective multiplicative factors; d) Corrected QTFs and smoothing of the values

Calibration of the pitch damping

Viscous pitch damping was added using a sensitivity analysis (Fig. 12):

a) Several values of quadratic damping are considered, numerical models are run with these different values and pitch RAOs are calculated.

b) The sum over the different sea states of the absolute value of the difference between the numerical and the experimental pitch RAO is calculated for each considered quadratic damping values. The sea states are separated between linear waves and steep waves. The relationship between the sum and the quadratic damping is highlighted by a second order polynomial fit line, and the minimum of this line is calculated, giving the optimum quadratic damping value.

This method assumes that the pitch linear damping value in the numerical model is correct. The RAOs for the corrected numerical model are plotted in Fig. 10 with blue squares. The addition of viscous pitch damping leads to a better fit of the modelled surge RAOs. The addition of pitch damping also improves the modelled heave RAOs near the pitch resonance.

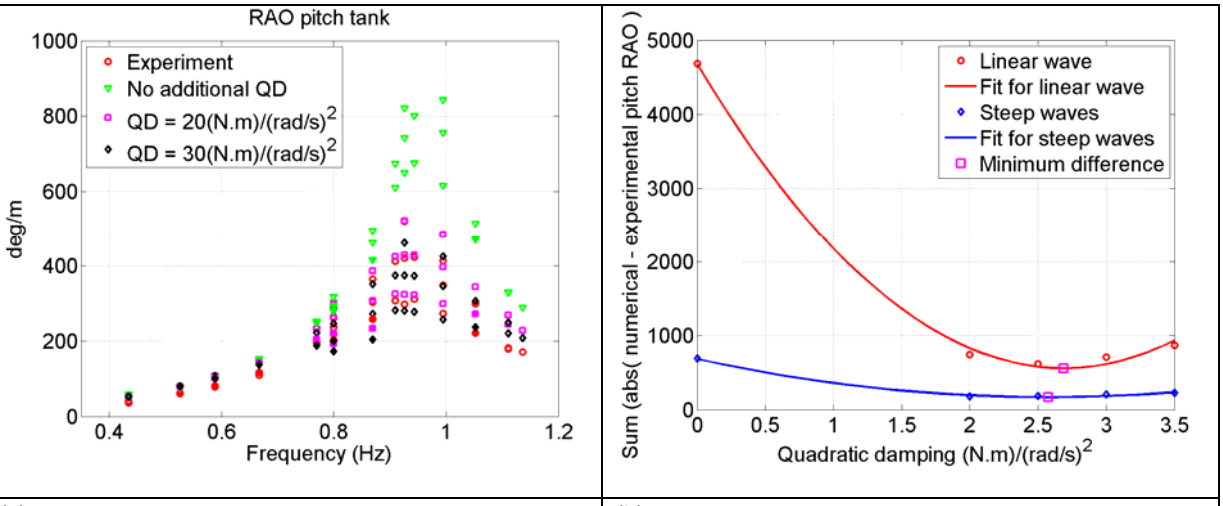

(a) (b)

Fig. 12 Sensitivity analysis for the pitch additional quadratic damping a) calculation of pitch RAO for different values of additional quadratic damping for all sea states QD stands for additional quadratic damping; b) minimisation of the sum of the absolute value of the difference between experimental and numerical pitch RAOs

After correction, the modelled RAOs, phases and mean drift are in good agreement with the experimental values. The amplitudes and phases of the corrected modelled RAOs indicate no significant difference in prediction for linear or steep waves.

3.4. Irregular wave tests

Irregular wave tests were used to validate the numerical model for realistic sea states. The wave elevation input signals for the tank were scaled time series of water surface elevation recorded during sea tests at the SWMTF. The inputs used for the numerical models were waves measured at 100Hz during the tank tests, filtered with a band pass filter with cutting frequencies of 0.15 and 2Hz (Fig. 13 (a)), and re-sampled at 4Hz to simplify Orcaflex™ calculations. Three different sea states (Table 7) were chosen, with a duration of approximately 500s each (model scale). The correlation coefficients between the experiment and the numerical model and the standard deviations for surge, heave and pitch motions as well as mooring loads were calculated for durations of 350s, in order to leave some initial time to let the model settle into its drifted position.

An example of wave elevation time-series, positions and mooring loads recorded during the experiment and computed by the numerical model is given in Fig. 13 (b), Fig. 14 and Fig. 15 respectively. The filtering of the waves removed spikes due to instrumentation but also slightly smoothed the elevation and modified the amplitude of some peaks or troughs. For example, in Fig. 13 at 135s, the measured elevation of the through was -0.059m when the filtered elevation was -0.067m. However, the correlation, evaluated with the covariance, between the measured and the input signal was over 0.99 for the three tests (Table 8). The heave and pitch motions are accurately replicated by the numerical model, shown in Fig. 14 (b) and (c). Correlation coefficients larger than 0.96 for the heave motion and 0.82 for the pitch motion support this finding, although the numerical model slightly under-damps the pitch motion. For example in case 2, the standard deviation of the experimental pitch motion was 5.1 deg when the standard deviation of the modelled motion was 5.4deg. This may be due to the fact that quadratic damping only was added to the system and linear damping could not be checked. Some differences can be observed in the surge motion, due to differences in the drift motion. In the example given in Fig. 14 (a), the buoy is reaching nearly the same minimum surge position; -0.063m for the experiment and -0.046m for the numerical model. Larger differences can be observed; for example, at t = 132s, the surge position is equal to 0.044m in the

experiment and 0.082m in the numerical model. Despite these inaccuracies, the correlation coefficients are always larger than 0.77 for the surge motion.

Mooring loads are compared between the tank tests and the numerical model in Fig. 15 and Table 8. These indicate that loads are replicated with a correlation coefficient over 0.75. Loads are slightly underestimated by the model, as shown by the standard deviations. For example, for case 2, the standard deviation in Line 1 was 1.7N for the experiment when it was 1.3N for the numerical model. This may be due to the underestimation of the surge motion. Maximum mooring loads are compared in Table 9. For example, the maximum mooring load on line 1 for case 2 was 27.4N for the experiment and 25.9N for the numerical model. These results indicate that the numerical model, in this setup, tends to underestimate the mooring loads, by 17% in the worst case.

Table 7 Properties of the irregular sea states

Case	*Hs* (m)	*Tp* (s)
1	0.23	1.88
2	0.10	1.30
3	0.29	2.91

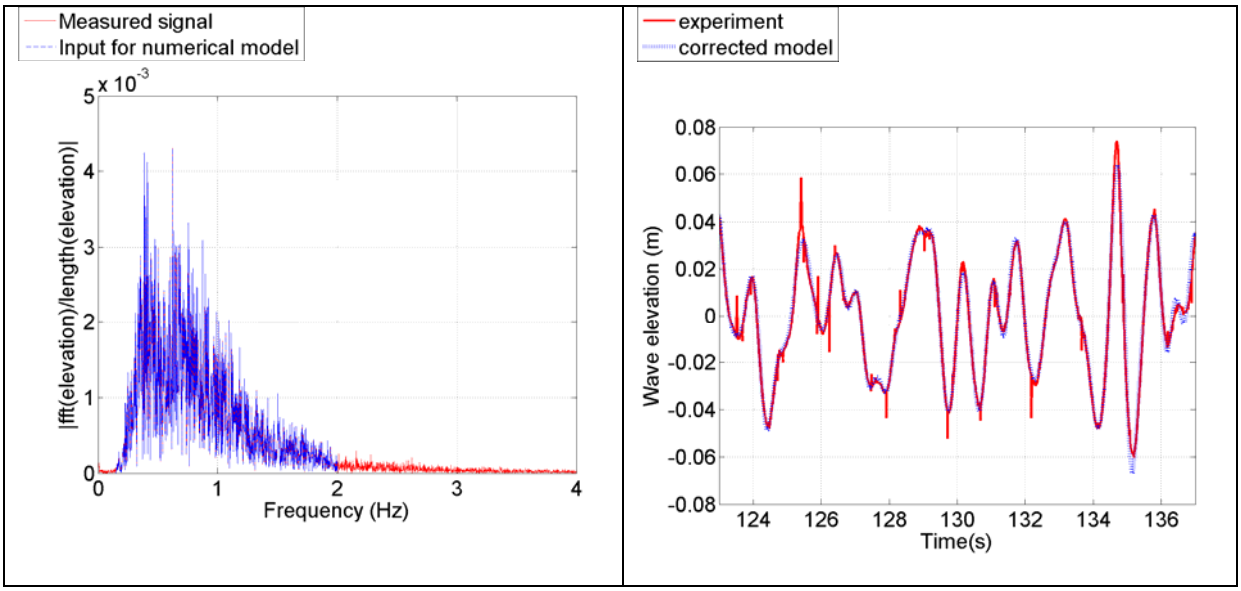

Fig. 13 Example of a) fft and filtered numerical model input and b) time series of wave elevation as measured during the experiment (red), and as input in the numerical model (blue) for Case2

Table 8 Comparison of experimental measurements and numerical model results for the wave elevation, buoy motions and mooring loads

	Wave	motion			Load in mooring line		
Correlation coefficients between the experiments and the numerical model							
Case	**Elevation**	**X**	**Z**	**pitch**	**Line 1**	**Line 2**	**Line 3**
1	0.99	0.79	0.96	0.91	0.76	0.84	0.77
2	0.99	0.93	0.96	0.92	0.83	0.85	0.80
3	0.99	0.77	0.96	0.82	0.75	0.79	0.75
Standard deviations: experiment/numerical model/relative error							
Case	**Elevation (m)**	**X (m)**	**Z (m)**	**Pitch**	**Line 1 (N)**	**Line 2 (N)**	**Line 3 (N)**
1	0.054/0.053/1%	0.12/0.070/41%	0.052/0.053/	6.2/7.2/15	2.7/2.0/28%	2.8/2.1/26%	2.8/2.0/29%
2	0.028/ 0.028/1%	0.073/0.053/27%	0.028/0.027/	5.1/	1.7/1.3/26%	2.2/1.6/27%	1.7/1.3/25%
3	0.077/0.078/1%	0.14/0.098/28%	0.077/0.078/	6.8/7.7/13	3.3/2.4/28%	3.2/2.4/23%	3.4/2.4/30%

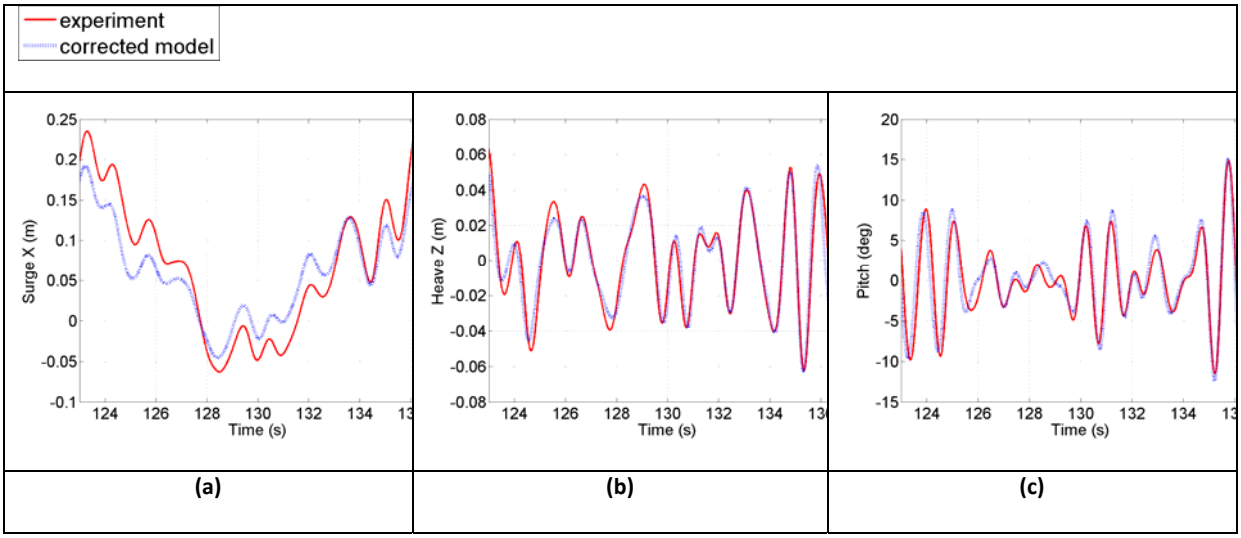

Fig. 14 Example of motion time series for Case 2: a) surge motion, b) heave motion and c) pitch motion

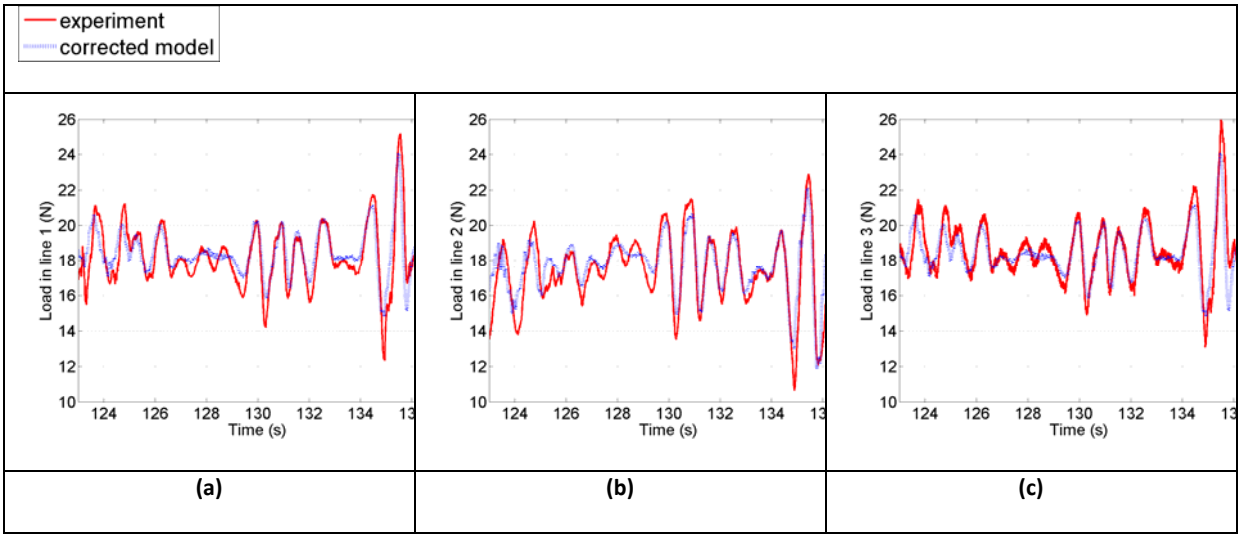

Fig. 15 Example of mooring load time series for Case 2: a) in the front line 1, b) in the back line 2, c) in the other front line 3.

Table 9 Comparison of maximum mooring loads for the different cases and the different mooring lines

Case		Line 1 (N)	Line 2 (N)	Line 3 (N)
1	Experiment	33.9	31.2	34.9
	Corrected Model.	28.9	25.2	28.9
	Relative error	15%	8%	12%
2	Experiment	27.4	25.0	27.7
	Corrected Model.	25.9	23.7	28.2
	Relative error	17%	5%	6%
3	Experiment	32.9	29.8	33.7
	Corrected Model.	28.9	25.2	28.9
	Relative error	17%	9%	14%

4. Discussion

The paper has presented a range of experimental investigations that validated the numerical model. These investigations give insight into specific and more general aspects.

i) From specifics to generals…

The results show in general a good agreement, with a few discrepancies: the mean drift is not accurately modelled, which was also the case with a similar buoy during experiments performed by Cozjin ([22]). The relative error between the standard deviations of the experimental and model pitch motion is between 5 and 15% and the maximum mooring loads are underestimated by 5 to 17%. Additional irregular wave tests, covering a more varied range of wave conditions, would provide greater confidence in the results driven by the mean drift force.

A radiation/diffraction potential analysis has been used to provide hydrodynamic input parameters to the numerical model. The main limitation of this theory is that it does not include viscous effects. It may also be difficult to replicate a complex shape in the radiation/diffraction potential model, and then a simplified shape of the hull can be used, but does introduce inaccuracies for added mass and radiation parameters. Cozjin [22] also noticed that the heave and pitch added mass were underestimated by a linear radiation-diffraction potential code for a similar buoy, and suggests that it is due to the fact that rotational accelerations are not taken into account by this kind of code.

A method has been developed in this paper to adjust added mass, radiation damping and viscous damping, based on results from decay tests. However, for the pitch decay tests, the pitch motion was coupled with the surge motion and the relative contribution of pitch radiation and viscous damping could not be determined experimentally. Because of this, the pitch radiation damping was assumed to be correct, and the pitch viscous damping was corrected using the pitch RAO plot from the regular wave tests. Another solution would have been to run forced oscillation tests to isolate the pitch motion.

Scaling effects are minimised by using a relatively large scale, and ensuring that the Reynolds number is similar for the model scale, and for the full scale device. However, it was not possible to find a rope with an exact 1:5 Froude scale stiffness. Fig. 16 compares numerical models for Case 2 using different rope stiffness, up to 10 times smaller or 100 times higher than the stiffness used in the final model. The correlation coefficients between the original and the modified models for the mooring loads drop down to 0.85 when the stiffness is divided by 10 (Fig. 16 (a)), but no significant changes are observed in terms of motions and loads otherwise. Similarly, the relative error between the standard deviation of the mooring loads increases when the stiffness is divided by 10 (Fig. 16 (b)). The maximum modelled mooring loads also dropped down to 22.4N in line 1 for the most compliant rope when this load was equal to 23.7N with the final model. These results indicate than when no accurate information is available on the stiffness of the mooring rope, it is better to choose a stiffer rope than what is desired, and that this will not have a significant consequence on the results.

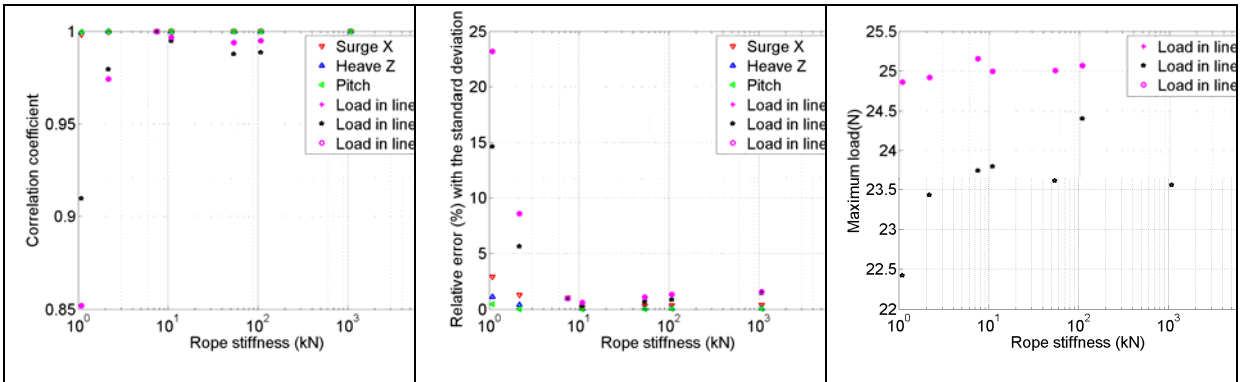

(a) (b) (c)

Fig. 16 Variations in motions and loads for Case 2 with models using different rope stiffness: a) Correlation coefficient between the model with a given stiffness and the model used in this study; b) Relative error between the standard deviation of motions and loads between the model with a given stiffness and the model used in this study; c) Maximum mooring load with the models using different stiffness

The aim of this numerical model is to gain a better understanding of dynamics of mooring system of wave energy devices in real conditions, using the SWMTF as a case study. The methodology used in this paper can be used for similar wave energy mooring tank tests. However, in comparison with a genuine wave energy device, the SWMTF does not have a power take-off, which will provide additional damping and make the motion of the buoy less dynamic.

The tank tests did not take into account some changes which occur in real sea conditions. For example, the variations in water depth were not covered; these variations lead to change in pre-tension and consequently change in the behaviour of the mooring system. The tidal range to nominal water depth ratio is 20% at the SWMTF, and approximately 10% at a full scale facility [10]. Hence tank tests and numerical models are complementary: Tank tests determine the hydrodynamic behaviour of the floating structure and mooring; numerical models allow the variation of those parameters that were fixed or not explored in the tank.

It should be noted that the presented tank tests were not conducted to estimate the behaviour in extreme conditions, i.e. to explore the survivability of the device, but to analyse the operational behaviour characteristics. At the SWMTF, 1-year return period sea state has an estimated significant wave height Hs of 3.5m and peak period Tp of 7s [23]. At the 1:5 scale used in this model, this corresponds to Hs equal to 0.7m and Tp to 3.1s. Hydrodynamics parameters have been calculated for this range of sea states. Whilst the tank tests do not cover this range of frequency they allow investigating the behaviour of the buoy in steep waves. For low frequencies, the RAOs (Fig. 10) and mean drift curves (Fig. 9) converge to a constant value, with the floating structure expected to follow the waves. The results can then be extrapolated with some confidence.

5. Conclusions and further work

This paper describes the detailed validation of a numerical model of a wave energy mooring system using tank test results. The mooring system used for this study was a 1:5 scale model catenary mooring system made of chains and representations of nylon mooring ropes. Static and quasi-static tests were used to check the buoy draft and the tension characteristics of the mooring system. The decay tests were used to estimate the overall damping and the added mass of the system. Regular wave tests were used to obtain the buoy motion RAOs, their phases and the buoy mean drift. The irregular wave tests have been performed to replicate real sea conditions at model scale, and to compare experimental with modelled results for motions and mooring loads. Results for irregular wave tests validate the numerical model for representative operational sea conditions. Despite some inaccuracies, which have been quantified, such a model validation gives much needed confidence in the ability of the numerical model to predict mooring loads at an early design stage.

The numerical model presented here will be used for further research into mooring systems, for example to improve the understanding of extreme mooring loads. In particular, further tank tests have been conducted using different materials in order to simulate marine growth and assess the different parameters associated with it: change of mooring stiffness, addition of mooring mass, increase in mooring line diameter and drag coefficient. This model can also be used to improve the understanding of the full scale SWMTF mooring system. Simulating real wave conditions will allow a better understanding of the mechanisms involved in extreme mooring loads, for example wave grouping or acceleration in buoy movements. However, several barriers have been highlighted; for example; the anchor position [24] was not accurate at the full scale facility, leading to a different pre-tension at the facility than the design one. At the moment, the model can be used as a reference before conducting any engineering changes at the full scale facility, for example changing the rope materials.

The methodology presented in this paper can be used by wave energy developers in the development of cost effective mooring systems which will contribute to the efficiency of wave energy devices. Numerical models contribute to improve the understanding of the mooring behaviour, to reduce the unknowns and consequently build a cost-effective mooring system, specifically designed for a given wave energy device and installation site.

6. Acknowledgments

The authors acknowledge the support of the MERiFIC project partners (Marine Energy in Far Peripheral and Island Communities, http://www.merific.eu) and of MARINET, a European Community Research Infrastructure Action under the FP7 Capacities Specific Programme (www.fp7-marinet.eu).

The authors would like to acknowledge the support of the South West Regional Development Agency for its support through the PRIMaRE institution and the support towards the FabTest through the Regional Growth Fund.

The authors are grateful for the valuable support of the Ifremer team: Emmanuel Mansuy, Aurélien Tancray, Christophe Maisondieu and Peter Davies.

The authors also want to thank Orcina for their technical support.

7. References

[1] Bedard R, Hagerman G, Previsic M, Siddiqui O, Thresher R, Ram B. Offshore wave power feasibility demonstration project, EPRI; 2005

[2] Carbon Trust and Black & Veatch. Accelerating marine energy. The potential for cost reduction – insights from the Carbon Trust Marine Energy Accelerator; 2001

[3] Harris RE, Johanning L, Wolfram J. Mooring systems for wave energy converters: a review of design issues and choices. In: Proceedings of International Conference on Marine Renewable Energy (MAREC), Blyth, UK; 2004

[4] Forestier JM, Holmes B, Barrett S, Lewis AW. Value and Validation of Small Scale Physical Model Tests of Floating Wave Energy Converters, In: Proceedings of 7th European Wave and Tidal Energy Conference (EWTEC), Porto, Portugal; 2007

[5] Vicente PC, Falcão AFO, Justino PAP. Non-linear Slack-Mooring Modelling of a Floating Two-Body Wave Energy Converter, In: Proceedings of 9th European Wave and Tidal Energy Conference (EWTEC), Southampton, UK; 2011

[6] Friis-Madsen E, Sørensen HC, Parmeggiani S. The development of a 1.5 MW Wave Dragon North Sea Demonstrator, In: Proceedings of 4th International Conference on Ocean Energy (ICOE), Dublin, Ireland; 2012

[7] Zanuttigh B, Angelelli E, Kofoed JP. Effects of mooring systems on the performance of a wave activated body energy converter, Renewable Energy, Vol 57, pp 422-431; 2013

[8] Fitzgerald J, Bergdahl L. Including moorings in the assessment of a generic offshore wave energy converter: A frequency domain approach, Marine Structures Vol 21, pp 23-46; 2007

[9] Harnois V, Parish D, Johanning L. Physical measurement of a slow drag of a drag embedment anchor during sea trials, In: Proceedings of 4th International Conference on Ocean Energy (ICOE), Dublin, Ireland; 2012

[10] Harnois V, Johanning L, Thies PR, Bjerke I. The influence of environmental conditions on the extreme mooring loads for highly dynamic responding moored structures, Submitted to Ocean Engineering; 2014

[11] Johanning L, Spargo AW, Parish D. Large scale mooring test facility – A technical note, In: Proceedings of 2nd International Conference on Ocean Energy (ICOE), Brest, France; 2008

[12] Weller SD, Davies P., Vickers AW and Johanning L. Synthetic Rope Responses in the Context of Load History: Operational Performance. Accepted for publication in Ocean Engineering

[13]Sharqawy MH, Lienhard V JH, Zubair SM. Thermophysical properties of seawater: a review of existing correlations and data, Desalination and Water Treatment, Vol 16, pp 354-380; 2010

[14]DNV. Offshore standard DNV-OS-E301, Position mooring; 2010

[15]Orcina. OrcaFlex manual; 2013

[16]Weller SD, Davies P, Vickers AW, Johanning L. Synthetic Rope Responses in the Context of Load History: The Influence of Aging. In review

[17]Le Roux D. MSc Thesis (in French) Rapport de Projet de fin d'études. Etude d'un ancrage textile pour la bouée SWMTF destinée à l'analyse du comportement des systèmes houlomoteurs. 2012

[18]Molin, B. Hydrodynamique des structures offshore; 2002

[19]WAFO group, WAFO A Matlab Toolbox for Analysis of Random Waves and Loads - A Tutorial, Math. Stat., Center for Math. Sci., Lund Univ., Lund, Sweden; 2000

[20]Faltinsen OM. Sea Loads on Ships and Offshore Structures, Cambridge University Press, Cambridge, UK; 1990

[21]Sarpkaya T, Isaacson M. Mechanics of wave forces on offshore structures.

[22]Cozijn JL, Uittenbogaard R, ter Brake E. Heave, Roll and Pitch Damping of a Deepwater CALM Buoy with a Skirt. In: Proceedings of the 15th International Offshore and Polar Engineering Conference, Seoul; 2005

[23]Johanning L, Spargo AW, Parish D. Large scale mooring test facility: A technical note. In: Proceedings of the 2nd International Conference on Ocean Energy (ICOE), Brest; 2008

[24]Harnois V, Parish D, Johanning L. Physical measurement of a slow drag of a drag embedment anchor during sea trials, In: Proceedings of 4th International Conference on Ocean Energy ICOE), Dublin; 2012